Journal of Rock Mechanics and Geotechnical Engineering 18 (2026) 3499–3511

Contents lists available at ScienceDirect

Journal of Rock Mechanics and Geotechnical Engineering

journal homepage: www.jrmge.cn

Full Length Article

Revisiting the Brazilian disc test with split Hopkinson pressure bar by high-speed digital image correlation analysis

Xiaofeng Li [a,b,*], Haibo Li [a], Giovanni Grasselli [b]

[a] Institute of Rock and Soil Mechanics, Chinese Academy of Sciences, Wuhan, 430071, China
[b] Department of Civil & Mineral Engineering, University of Toronto, Toronto, M5S1A4, Canada

ARTICLE INFO

Article history:
Received 15 April 2025
Received in revised form
6 June 2025
Accepted 18 August 2025
Available online 17 October 2025

Keywords:
High-speed digital image correlation (DIC)
Brazilian disc test
Critical valid strain rate
Rate dependency
Granitic rock

ABSTRACT

The ISRM-suggested Brazilian disc (BD) test using split Hopkinson pressure bar (SHPB) for dynamic rock tensile strength requires central crack initiation and stress equilibrium. This study aims to re-evaluate the critical strain rate, ensuring a valid dynamic Brazilian disc test, and to analyse the reliable dynamic tensile behaviour of granite using high-speed digital image correlation (DIC). The comparison between the measured strain obtained through high-speed DIC analysis and the strain gauge allowed for determining the optimal subset parameters used to obtain the real-time deformation field and the stress-strain curve from DIC data. Crack initiation, crack velocity, and failure process are studied to reveal the rate dependence of granites. A unified dynamic increase factor (DIF) model is proposed for the tensile strength of rocks, and the reason for the sudden drop in DIF for high strain rates is discussed. The results reveal that the upper limit of the valid strain rate, which ensures the validity of the ISRM-suggested dynamic BD test, is co-determined by the conditions of stress equilibrium and crack initiation from the centre of the disc. At higher strain rates (75 s^{-1}), BD test results fail to capture the actual tensile behaviour of rocks, and the potential factors influencing the critical valid strain rate (CVSr), such as sample radius and boundary crack length, should also be considered.

1. Introduction

Understanding the dynamic behaviour of rock material is of significance for underground excavation (Zhou et al., 2014), earthquake rupturing (Griffith et al., 2018), rock fragmentation (Grady and Kipp, 1980) and military prevention against projectile penetration (Schultz et al., 2007). The tensile strength of brittle materials is much lower than the compressive strength, making rocks more prone to tensile failure without significant associated deformation and cause dynamic disasters, e.g. the spalling in tunnels induced by reflected stress waves in blasts (Cai et al., 2012), the evident rate-dependent debris distribution determined by tensile fracturing initiated from initial defects (Hogan et al., 2015), and the pervasively pulverized rocks at grain scale due to isotropic tensile impacts during earthquakes (Griffith et al., 2018). Therefore, understanding the dynamic tensile behaviour of rocks is critical for studying the dynamic response of rock engineering under blast and seismic loading.

Characterising the dynamic tensile behaviour of rocks requires appropriate specimen configurations and reliable testing methods. During last few decades, the dynamic behaviour in tension for rocks tested using the SHPB has been well understood through the direct tension test (Howe et al., 1974; Goldsmith et al., 1976) the Brazilian disc (BD) test (Gomez et al., 2001; Zhang and Zhao, 2013a); the flattened BD test (Wang et al., 2006); the BD test with jaws (Dai et al., 2010a); the semi-circular bend test (Dai et al., 2010b); the spherical splitting test (Huang et al., 2014); and the spalling test (Kubota et al., 2008). Direct tension test is straightforward, but suffers from the difficulty of boundary bonding, and results in stress concentrations or eccentric tension loads near the sample ends (Heard et al., 2018). Due to the ease in sample preparation and low requirements on the loading apparatus, BD is suggested by the International Society for Rock Mechanics and Rock Engineering (ISRM) to determine the dynamic tensile

* Corresponding author. Institute of Rock and Soil Mechanics, Chinese Academy of Sciences, Wuhan, 430071, China.
E-mail addresses: xfli@whrsm.ac.cn, xiaofengli@utoronto.ca (X. Li).
Peer review under responsibility of Institute of Rock and Soil Mechanics, Chinese Academy of Sciences.

https://doi.org/10.1016/j.jrmge.2025.08.016

strength of rock materials (Zhou et al., 2012). But the prerequisites for a valid dynamic BD test are (a) stress equilibrium within the specimen, (b) one-dimensional stress wave propagation, and (c) crack initiation from the centreline of the disc. The test results are acceptable only when the sample is close to stress equilibrium, which requires around 5–10 round trips of the incident wave within the sample prior to fracture. Preliminary tests with high strain rates demonstrated that cracks initiated from damage zones in the vicinity of load platens, near the sample contact area, while the measured value of fracture strength is heavily influenced by the quality of the fixture (Gomez et al., 2001)), resulting in the following maximum allowable strain rates to achieve stress equilibrium: 1.0–5.0 s^{-1} for the concrete plain splitting test (Albertini and Montagnani, 1994); 20 s^{-1} for the BD test (Tedesco et al., 1993); 120 s^{-1} for the spalling test (Klepaczko and Brara, 2001); and 45 s^{-1} for the flattened BD test (Wang et al., 2006). Higher strain rates induce stress concentration beneath contact loading points, causing premature cracking at sample ends. This violates fundamental assumptions of the standard Brazilian disc (BD) test. Nevertheless, from the literature review of dynamic tensile tests on rocks in the last decades, as shown in Fig. 1, there are still many studies evaluating dynamic tensile strength beyond the limited strain rate range. In Fig. 1a, the black curve is the predicted dynamic increase factor (DIF) of tensile strength by fitting the unified dynamic strength model. The DIF, which is the ratio of dynamic tensile strength (σ_{td}) to static tensile strength (σ_τ), describes the strain rate effect on the failure strength, and has values theoretically >10 when the strain rate is close to 100 s^{-1}. However, the strength decreases with the increase of strain rate in region III^b, and DIF drops to 2–4 in a higher strain rate range. The critical strain rate dividing region II and region III is the maximum strain rate which can maintain the strain rate effect of rocks in tension. This phenomenon appears to be independent of the rock type tested, as demonstrated in Fig. 1b, since region III^b is commonly found in various rock types such as granite, sandstone, and dolomite, among others. As the data is regrouped according to the testing approach, the drop of strength in tension is evident in the BD test, shown in Fig. 1c. It is concluded that there is an upper limit to the range of reliable strain rates that can be measured by the ISRM-suggested method. The results will fail to characterise the actual dynamic response of rocks when the loading rate exceeds the limit range. Therefore, evaluating the validity of experimental results is crucial to determine the dynamic behaviour in the laboratory and remains to be solved herein.

In recent decades, there have been many attempts to explore uniform stress conditions and the validity of the dynamic BD test. For example, Gomez et al. (2001) used the photoelastic method to compare the stress equilibrium difference of Homalite-100 under quasi-static and dynamic loads and found that the failure pattern of the specimens was consistent in both static and dynamic BD tests. Other non-contact techniques, for example the laser measurement technique (Li and Ramesh, 2007), Moiré method (Zhang et al., 1999), caustic method (Field et al., 2004) and DIC (Chen et al., 2013; Zhang and Zhao, 2013a; Xing et al., 2018), were carried out to explore the mechanical properties and fracture processes of rock materials. Among these, DIC is a non-contact, non-destructive, powerful full-field method which is capable of tracking spatial and temporal displacement and the strain fields of materials (Peters and Ranson, 1982). However, research in extreme dynamic regimes involving high-strain-rate phenomena (>10^3 s^{-1}) such as impact, blasting, and Kolsky bar tests remains at a nascent stage of development. With the advantage of ultra-high speed (UHS) imaging technique, high-speed DIC is employed to understand the onset of fracturing and crack velocity (Zhang and Zhao, 2013a), full-field deformation (Chen et al., 2014; Fourmeau et al., 2014), strain localisation and fracturing mechanism (Yao et al., 2016),

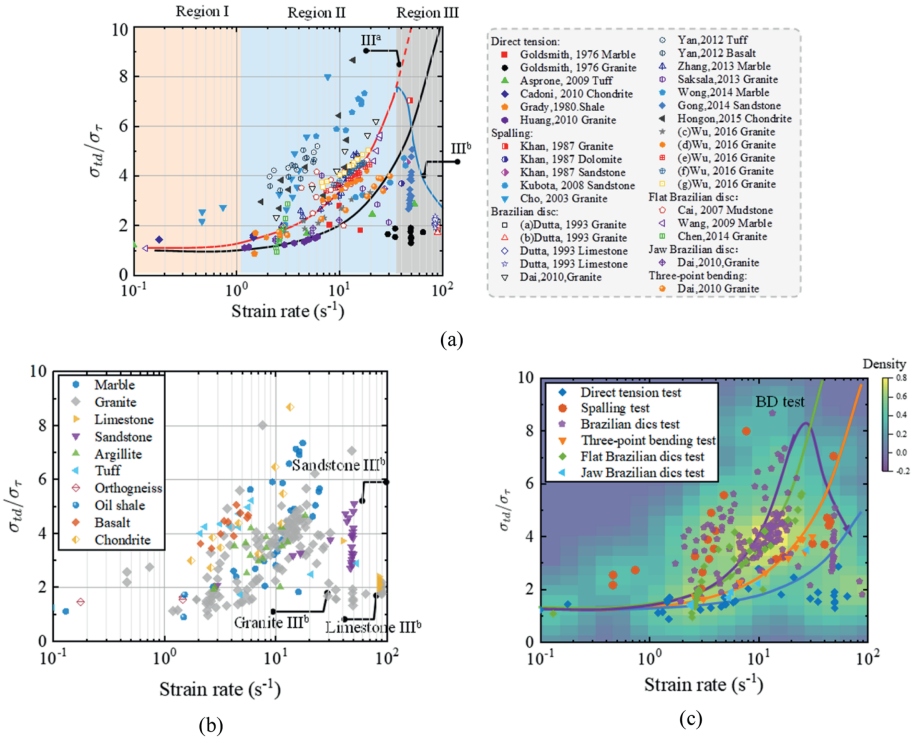

Fig. 1. (a) Dynamic tensile strength and DIF versus strain rate of rocks (Goldsmith et al., 1976; Grady and Kipp, 1980; Khan and Irani, 1987; Dutta and Kim, 1993; Cho et al., 2003; Cai et al., 2007; Kubota et al., 2008; Asprone et al., 2009; Wang et al., 2009; Cadoni, 2010; Dai et al., 2010a, 2010b; Dai and Xia, 2010; Huang et al., 2010a, 2010b; Yan et al., 2012; Saksala et al., 2013; Zhang and Zhao, 2013b; Chen et al., 2014; Wong et al., 2014; Wu et al., 2016), (b) DIF by rock type, and (c) DIF by test method.

dynamic toughness of notched semi-circular bend (Gao et al., 2015) and crack damage thresholds (Xing et al., 2018). The UHS camera is currently available at a recording frequency of up to one million frames of second and the deformation field is recorded at a temporal resolution of microseconds. Nevertheless, the application of high-speed DIC to simultaneously validate the BD methodology and characterise rate-dependent tensile behaviour in geological materials remains largely unexplored in experimental rock mechanics. Zhang and Zhao (2013a) employed the digital image correlation (DIC) technique for dynamic BD and obtained the real-time strain field for marble with the SHPB. Due to the strict assumptions required for the standard SHPB BD test, obtaining the full field strain is meaningful because the distribution and spatial localisation of strain gradient can be directly used to determine the crack initiation and propagation, which is impossible with conventional strain gauge methods (Pierron et al., 2011).

This study aims to address the questions: (a) "What are the actual dynamic tensile properties of granites, their rate dependency, and deformation fields measured using the DIC technique with a high-speed camera?" and (b) "What is the range of the critical valid strain rate (CVSr) that defines the validity of the BD test". To answer these two questions, BD tests using a Kolsky bar test are carried out on disc rock samples to re-evaluate the validity and the stress equilibrium state of BD method based on the transit displacement and strain fields for the first time. Then, the rate dependency of tensile strength is analysed by excluding invalid results induced by boundary failure and compared to the theoretical model to determine the characteristic strain rate. Finally, the critical strain rate and progressive failure patterns are discussed.

2. Methodology

2.1. Sample preparation

Granite, a typical brittle rock whose mechanical properties reflect most crystalline brittle rocks, is used for dynamic BD experiments in this study. The Electron Backscatter Diffraction (EBSD) technology and thin section image are employed for mineralogy analysis as discussed in our previous study (Li et al., 2021). By injecting an accelerated electron beam into the sample and analysing the diffracted backscattered electrons, EBSD technology can obtain the information of crystal microstructure in high resolution, enabling effective identification of mineral phases and their crystallographic orientations. According to the results, the main mineral constituents of the samples are quartz (Qtz), soda feldspar (Soda Fsp), plagioclase, mica (ma) and accessory minerals (<0.4 %), including hornblende, pyroxene, and garnet. The content ratio of different minerals can be obtained from thin section and Electron Backscatter Diffraction (EBSD) images, as shown in Fig. 2a and b (see details in Table 1). The result shows the average grain sizes of Qtz, Fsp, and ma are 1.88 mm, 2.64 mm and 0.85 mm, respectively. The orientation distribution of grain boundaries from the granite sample is depicted in Fig. 1c. The result shows no evident anisotropic fabric with preferred beddings in the specimen, and most minerals are uniformly distributed with a probability frequency approximating 3.0 %.

All samples are cored into disks with a diameter of 50 mm and a thickness of 25 mm. The thickness/diameter ratio is set as 0.5 to minimise the inertia effect and to reduce the effect of thickness on the tensile strength. In addition, the maximum grain size (4.54 mm) is less than 1/10 of the diameter (50 mm), so the grain size effect on strength can be neglected according to the ISRM

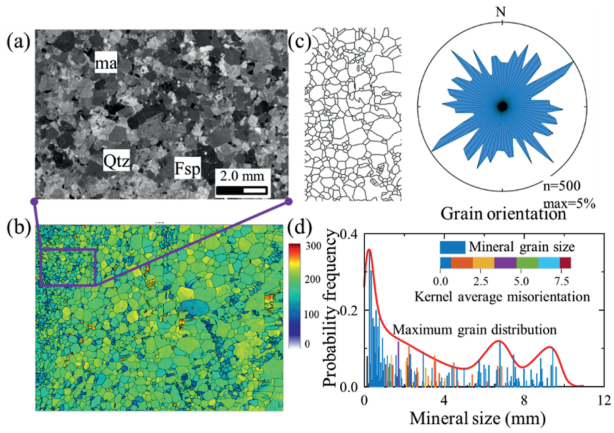

Fig. 2. (a) Thin section images of a representative granite sample, Quartz-Qtz; Feldspar-Fsp; Mica-ma. (b) Rock digitisation of the EBSD grain orientation map, (c) the orientation distribution of the grain boundaries in the granite sample, and (d) the grain size distribution.

suggestion. The static experiments are performed on an MTS-815 apparatus at a strain rate less than 5×10^{-5} s^{-1}. In order to avoid any size effect on laboratory tests, all samples for both dynamic and static tests have the same dimensions. The quasi-static experimental results indicate that the Young's modulus of this granite is (54.6 ± 3.7) GPa, and Poisson's ratio is 0.19 ± 0.04. The average values for uniaxial compressive strength (UCS) and Brazilian tension strength (BTS) are 192 MPa and 11.4 MPa, respectively.

2.2. Loading configuration and testing method

Dynamic experiments are conducted with SHPB, and the diagram of the apparatus is shown in Fig. 3. The setup consists of a loading system, high-speed camera system, and strain measurement system. The loading system includes the incident bar, transmitted bar, and the striker, which are made of 48CrMoA steel with a diameter of 50 mm and lengths of 300 mm, 2500 mm and 2500 mm, respectively. As the oscillation induced by the sharp rising of the incident wave would result in difficulty in reaching stress equilibrium in the rock sample, a pulse shaping technique, by changing the dimension of a rubber pulse shaper, is used to minimise the influences of dispersion and inertia in this study.

The high-speed camera and conventional strain gauges are used to monitor the deformation signals across the sample. During the test, the tensile wave is reflected when the incident wave reaches the end of the incident rod while the rest continues to travel through the sample towards the transmitted bar. All signals are recorded by strain gauges mounted on incident and transmitted bars. The signals are amplified by a Wheatstone bridge and stored using an oscilloscope (Fig. 3a). The subscripts in, re, and tr represent the incident, reflected and transmitted waves, respectively. The forces at the ends of the sample are

$$\left.\begin{aligned} P_{\mathrm{lef}}(t) &= E_b A_b[\varepsilon_{\mathrm{in}}(t) + \varepsilon_{\mathrm{re}}(t)] \\ P_{\mathrm{rig}}(t) &= E_b A_b \varepsilon_{\mathrm{tr}}(t) \end{aligned}\right\} \quad (1)$$

where E_b is the elastic modulus of the rod, A_b is the area of the bars. $P_{\mathrm{lef}}(t)$ and $P_{\mathrm{rig}}(t)$ are forces at the left and right ends of the sample, respectively. The forces are balanced when the stress equilibrium in the sample is achieved. Therefore, the maximum vertical tensile stress located at the centre of the disk is determined as

Table 1
Mineral composition and grain size of granites.

Mineral	Chemistry ingredient	Content (%)	Minimum size (mm)	Maximum size (mm)	Average size (mm)
Quartz	SiO_2	32.7	0.86	2.45	1.88
Feldspar	$NaAlSi_3O_8$, $KAlSi_3O_8$	52.6	1.46	4.54	2.64
Mica	$K_3Si_3O_{10}$	14.3	0.28	1.54	0.85
Others	*	0.4	0.08	0.45	0.34

Note: * includes hornblende, pyroxene, and garnet.

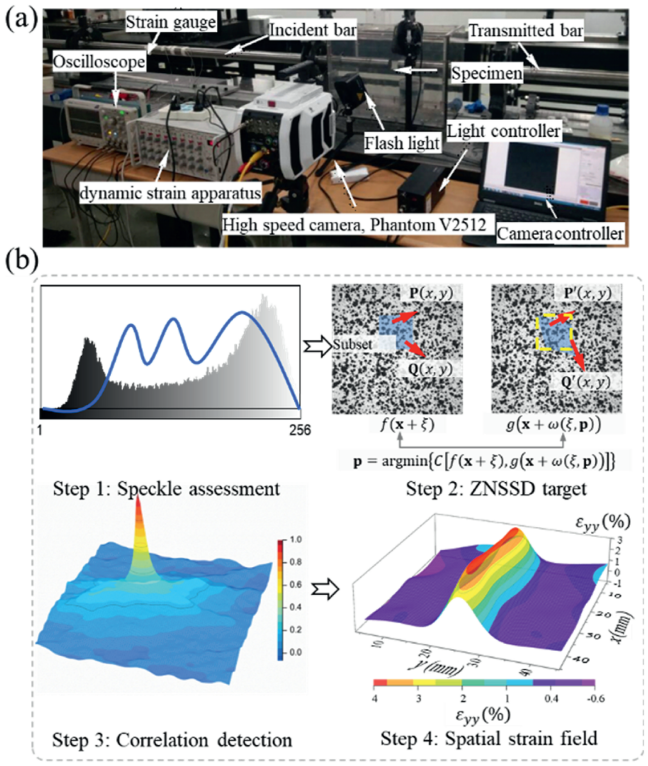

Fig. 3. (a) Diagram of SHPB apparatus. (b) The processing of high-speed DIC.

$$\sigma_t = \frac{2P(t)_{max}}{\pi d_s b_s} = \frac{\left[P_{lef}(t) + P_{rig}(t)\right]_{max}}{\pi d_s b_s} \tag{2}$$

where σ_t is the tensile strength and $P(t)_{max}$ coincides with the maximum force when the failure occurs. d_s and b_s are the diameter and thickness of the sample. The stress rate and strain rate are computed by

$$\dot{\sigma}_t = \frac{\sigma_t}{t_p}, \dot{\varepsilon}_t = \frac{\dot{\sigma}_t}{E} \tag{3}$$

where t_p is the loading time corresponding to the peak force $P(t)_{max}$ and E is the elastic modulus of the sample in tension.

2.3. High-speed digital image correlation (DIC)

A CMOS UHS camera was used to acquire the digital images during the loading process. As shown in Fig. 3b, the region of interest (ROI) of the camera is 50 mm × 50 mm, and the magnification factor is 0.195 mm per pixel. In order to obtain an optimised speckle pattern, the mean intensity gradient suggested by Pan et al. (2010) is used in this study. To record the cracking propagation, three strain gauges with a resistance value of 120 Ω are mounted on the back of the sample. The horizontal space between the strain gauges is 15 mm, and their orientation angle is 90°.

The DIC algorithm finds the optimal matching subsets in the reference and deformed digital images. Different from the static loading, the rock undergoes large displacement and background noise under impact loads. The cross-correlation function Zero-Normalised Sum of Squared Differences (ZNSSD) with strong anti-interference ability is used for high-speed tests; the correlation coefficient C_Ω of ZNSSD will not change even when the light intensity in ROI changes

$$C_\Omega = \sum_{\boldsymbol{p}\in\Omega}\left[\frac{g^{ref}(\boldsymbol{x}) - g_m^{ref}}{\Delta g^{ref}} - \frac{g^{def}(\boldsymbol{x} + \boldsymbol{u}(\boldsymbol{x}, \boldsymbol{u}_\Omega)) - g_m^{def}}{\Delta g^{def}}\right]^2 \tag{4}$$

where $\boldsymbol{p}$ is the point in the subset (central point is x_0, y_0) with position of $\boldsymbol{x}$, Ω is the subset zone, and g^{ref} and g_m^{ref} are the grey values of $\boldsymbol{p}$ before and after the deformation, respectively. $\boldsymbol{u}$ is the displacement vector, which is a function of $\boldsymbol{x}$ and $\boldsymbol{u}_\Omega$. $\boldsymbol{u}_\Omega$ is the displacement vector of the subset zone Ω.

For simplicity, the first-order displacement function is used in this study

$$\begin{aligned} &\forall(\boldsymbol{x}) \in \Omega, \exists\left(\boldsymbol{u}_{\Omega,m}\right)_{m\in[1,6]} \in \mathbb{R}^6, \\ &\left.\begin{aligned} \boldsymbol{u}_1(\boldsymbol{x}, \boldsymbol{u}_\Omega) &= \boldsymbol{u}_{\Omega,1} + \boldsymbol{u}_{\Omega,3} \times \Delta\boldsymbol{x} + \boldsymbol{u}_{\Omega,5} \times \Delta\boldsymbol{y} \\ \boldsymbol{u}_2(\boldsymbol{x}, \boldsymbol{u}_\Omega) &= \boldsymbol{u}_{\Omega,2} + \boldsymbol{u}_{\Omega,4} \times \Delta\boldsymbol{x} + \boldsymbol{u}_{\Omega,6} \times \Delta\boldsymbol{y} \end{aligned}\right\} \end{aligned} \tag{5}$$

The Newton-Raphson method is used to optimise the equation for each subset as

$$\forall\Omega, \left(\boldsymbol{u}_{\Omega,m}\right)_{m\in[1,6]} = \mathrm{Argmin}(C_\Omega(\overline{\boldsymbol{u}}_\Omega)), \ \overline{\boldsymbol{u}}_\Omega \in \mathbb{R}^6 \tag{6}$$

While each component satisfies

$$\forall m \in [1, 2, \cdots, 6], \ \frac{\partial C_\Omega(\overline{\boldsymbol{u}}_\Omega)}{\partial \boldsymbol{u}_{\Omega,m}} = 0 \tag{7}$$

The strain in the field can be computed as

$$\left.\begin{aligned} \varepsilon_{xx} &= \boldsymbol{u}_{\Omega,3} + \frac{1}{2}\left(\boldsymbol{u}_{\Omega,3}^2 + \boldsymbol{u}_{\Omega,4}^2\right) \\ \varepsilon_{yy} &= \boldsymbol{u}_{\Omega,6} + \frac{1}{2}\left(\boldsymbol{u}_{\Omega,5}^2 + \boldsymbol{u}_{\Omega,6}^2\right) \\ \varepsilon_{xy} &= \frac{1}{2}\left(\boldsymbol{u}_{\Omega,4} + \boldsymbol{u}_{\Omega,5}\right) + \frac{1}{2}\left(\boldsymbol{u}_{\Omega,3} \times \boldsymbol{u}_{\Omega,5} + \boldsymbol{u}_{\Omega,2} \times \boldsymbol{u}_{\Omega,6}\right) \end{aligned}\right\} \tag{8}$$

The subpixel interpolation based on the bicubic spline is

$$g(\overline{\boldsymbol{x}}) = \sum_{i=0}^{3}\sum_{j=0}^{3} N_{ij} x_i \times x_j \tag{9}$$

where N_{ij} is the coefficient determined by the grey-scale values of the point. $\overline{\boldsymbol{x}}$ is an arbitrary point position vector in the subset zone.

The detailed algorithm of the local DIC used in this study can be found in Algorithm 1.

Algorithm 1. Calculation procedure of local subset DIC

1	Input the reference image g^{ref}, deformed image g^{def}, subset size, size step, estimate displacement
2	Use a coarse-fine search approach to find the optimum initial integer displacement
3	Compute the subpixel interpolation
4	Set the initial displacement $\boldsymbol{u}_{\Omega}^{0}$ and the displacement gradient $u_{1,1}u_{2,1}u_{1,2}u_{2,2}=0$
5	Warp the deformed image with the initial displacement
6	Compute the first gradient $\nabla C(\boldsymbol{u}_{\Omega})$ and Hessian matrix $\nabla\nabla C(\boldsymbol{u}_{\Omega})$ while $\left\|C^{n+1}-C^{n}\right\|>\varepsilon$
7	Compute the current displacement using $\boldsymbol{u}_{\Omega}^{n+1}=\boldsymbol{u}_{\Omega}^{n}-\frac{\nabla C(\boldsymbol{u}_{\Omega})}{\nabla\nabla C(\boldsymbol{u}_{\Omega})}$ while $\left\|C^{n+1}-C^{n}\right\|>\varepsilon$
8	Subpixel interpolation considering the displacement at step n while $\left\|C^{n+1}-C^{n}\right\|>\varepsilon$
9	Warp deformed image with current displacement $\boldsymbol{u}_{\Omega}^{n+1}$ while $\left\|C^{n+1}-C^{n}\right\|>\varepsilon$
10	Return Displacement vector $\boldsymbol{u}_{\Omega}$ of each subset

3. Results

3.1. Stress equilibrium

To evaluate the stress difference at two ends of the sample, the stress equilibrium factor, which is a dimensionless ratio of the stress difference to the average stress, is computed

$$\eta_{\sigma}=2\left|\frac{\sigma_{\mathrm{in}}+\sigma_{\mathrm{re}}-\sigma_{\mathrm{tr}}}{\sigma_{\mathrm{in}}+\sigma_{\mathrm{re}}+\sigma_{\mathrm{tr}}}\right| \tag{10}$$

The sample can be considered in stress equilibrium when η_{σ} is less than 5.0 % (Ravichandran and Subhash, 1994). The challenge of this method is the uncertainty in determining the arrival time of reflected and transmitted waves and the error associated to the three-wave aligning process by the human operator. At a lower impact velocity, e.g. $v_{\mathrm{s}}=5.6$ m/s, the stress difference at the ends of the sample is nearly eliminated. From the stress equilibrium factor as shown in Fig. 4b, the sample is balanced during the whole process of loading, which is confirmed by both the three-wave method and the stress equilibrium factor. As a typical example to distinguish the difference between these two methods, Fig. 4c and d plots the history stresses at the ends of the sample as well as the stress equilibrium factor when the impact velocity is 8.7 m/s. It is hard to obtain a balanced stage by comparing the stress state at the ends of the sample, as shown in Fig. 4c. This result violates the conclusion obtained by the three-wave method. As marked in Fig. 4d, the balanced state was achieved only in a range from 75 μs to 100 μs. That means the equilibrium hypothesis within the sample is only reached for a short period prior to peak stress, and this stage will be significantly shortened when the loading rate is increased. The critical loading rate, which determines the reasonability of stress equilibrium and central crack initiation, will be fully discussed in the following section.

3.2. Sensitivity of DIC subset parameters

In local DIC, the subset size is coupled with the speckle characteristics and plays a great role in the displacement calculation. If the grey pattern has low levels of noise, the choice of a small subset size will introduce a higher variability in the measured displacement. In order to obtain the optimal subset size for DIC analysis of dynamic BD, four subset sizes were chosen for strain analysis and the results compared. The subset size varied from 10 pixels to 40 pixels at a step size of 5 pixels, and the results of the maximum principal strain field are shown in Fig. 5a. The subset size suggested by the International Digital Image Correlation Society (Jones and Iadicola, 2018) should contain a minimum of three speckles, as a smaller subset will result in insufficient filtering for the strain results of the DIC virtual strain gauge. The results indicated that the subset size of 20 shows less mean bias error than the size of 10, while not over-filtering the strain. The tensile strains on the centreline performed by different subset sizes are plotted in Fig. 6a. The larger subsets will decrease the values of measured strain and result in a smoother strain field. The strain distribution is excessively discrete as the subset size is 10, and the comparison between DIC results with strain gauge will be discussed in the following section.

The subset step determines the density of pixels at which DIC data is computed and influences the resolution of the measurements. Four subset step sizes, $s=1$, 5, 7 and 10, are chosen to obtain the optimal subset step. The increase of the subset step-size will increase the overlap between two neighbouring subsets, and the tensile strain on the centreline with different step sizes is compared in Fig. 6b. An "oversized" step-size will over-interpolate the measurements and increase the bias to determine the crack tips. However, decreasing the step size further does not improve the resolution of measurements as expected and consumes more computational time.

3.3. Calibration of DIC results with strain gauges

We further compared the tensile strain obtained by DIC analysis with the strain gauge measurement. A virtual strain gauge is set at the middle point of the Brazilian disc with a length l_d. The orientation of the strain gauge is perpendicular to the loading direction, and the crack opening displacement (COD) is the difference in the vertical displacement between two points. To avoid the disturbance of the displacement discontinuity, a displacement gradient of the virtual strain gauge is defined as:

$$g_{yy}(i)=\frac{\partial v}{\partial y}=\frac{v(i+1)-v(i)}{2d} \tag{11}$$

where d is the spacing of subsets and i is the subset id on the virtual strain gauge. v is the velocity of the i th subset. The comparison of tensile strain between the strain gauge method and DIC analysis is plotted in Fig. 7. The prerequisite of the stress wave method is that the sample is well contacted with the rods. That is only satisfied during the loading period prior to peak stress. After the failure of the sample, the transmitted stress is unloaded, but the tension deformation (red curve) in the specimen is still increasing. The strain measured by the strain gauge is identical to the results obtained by the one-wave method and three-wave method, as shown in Fig. 7. The subset size of 20 shows a better match with the strain gauge measurement and therefore is chosen as the optimal size for further DIC analysis. The strain value

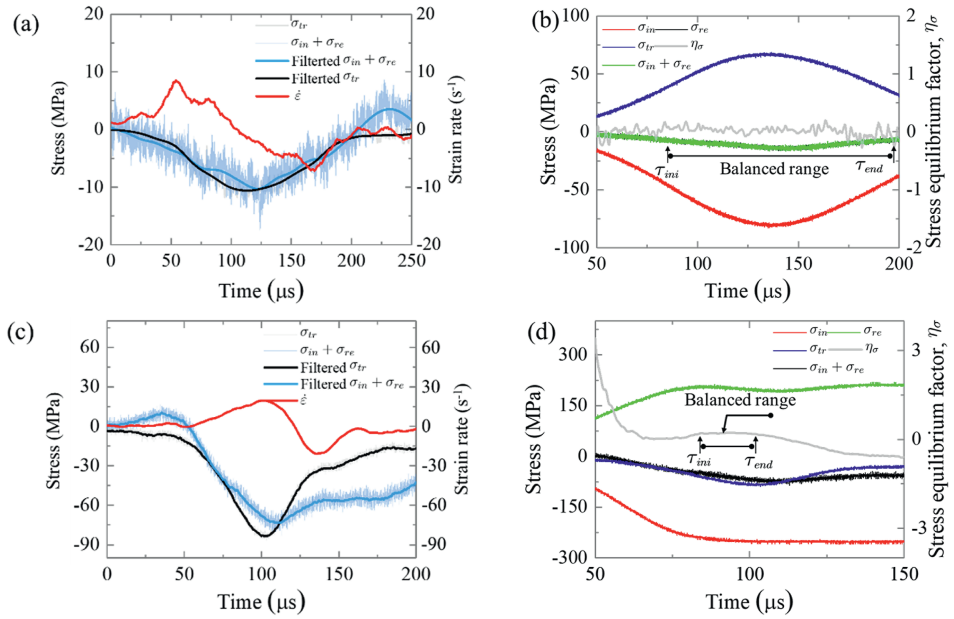

Fig. 4. (a), (c) Variance of the stresses and strain rate at two ends of the typical rock samples GB-3-5.6 and GB-8-8.7 and (b) and (d) dynamic three-wave stress equilibrium.

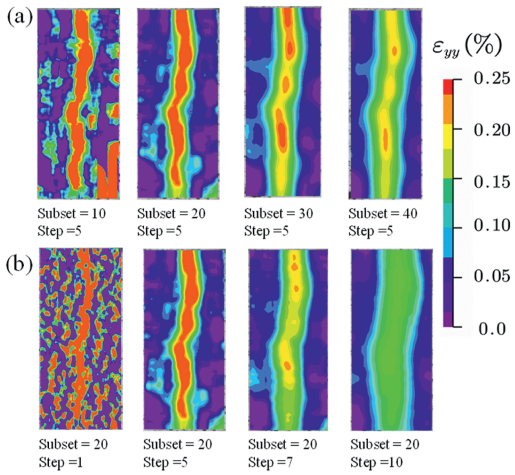

Fig. 5. (a) Effect of subset size and (b) subset step on the maximum principal strain for determining the crack propagation in the ROI.

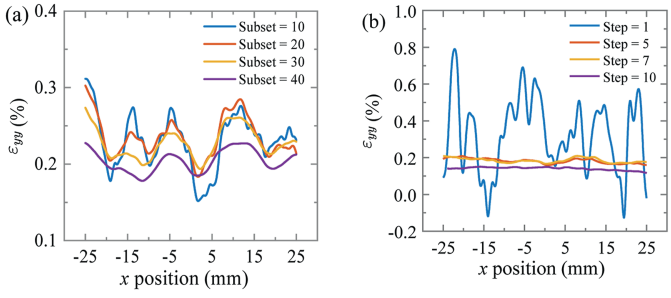

Fig. 6. (a) Effect of subset size and (b) subset step-size on the tensile strain distribution along the centreline crossing the horizontal crack.

measured by DIC is larger than that calculated from the stress wave method because (a) the strain calculated from the stress wave method is an average value on the centreline, and (b) the

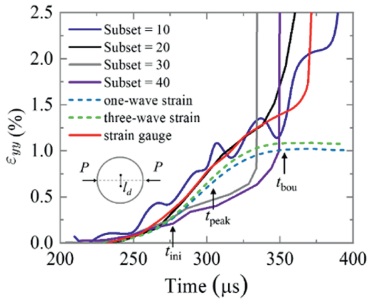

Fig. 7. Comparison of different strain results computed from one-wave method, three-wave method, and direct strain gauge and DIC analysis.

strain recorded by the stress wave method in the post-peak stage is not the actual deformation of the sample, as the sample is separated from the rods. That means the stress equilibrium checked by the three-wave method is valid only when the sample is in perfect contact with the rods.

3.4. Displacement and strain fields from DIC analysis

Fig. 8 shows the results of displacement for rock sample GB-3-5.6 at different stress levels. The zone of camera (ZOC) is 256 × 256 pixels, and the zone of interest (ZOI) is 240 × 80 pixels. The optimal subset size and subset-step size are set to 20 and 5, respectively. From Fig. 8b, the stress difference is eliminated at the peak stress moment. The platform after the peak strain rate implies that the sample at the moment corresponding to peak stress is balanced. The peak strain rate corresponds to the moment that the crack initiates from the sample centreline, where the maximum principal strain is 0.32 %.

From the fields of displacement shown in Fig. 8a, the stress propagation from left to right can be evidently captured. The stress level of crack initiation is about 0.9 σ_p, and after that, the stress wave continues to propagate to the end of the sample and resulting in an increase in the transmitted stress. The vertical displacement displays the rupture in the horizontal centreline and

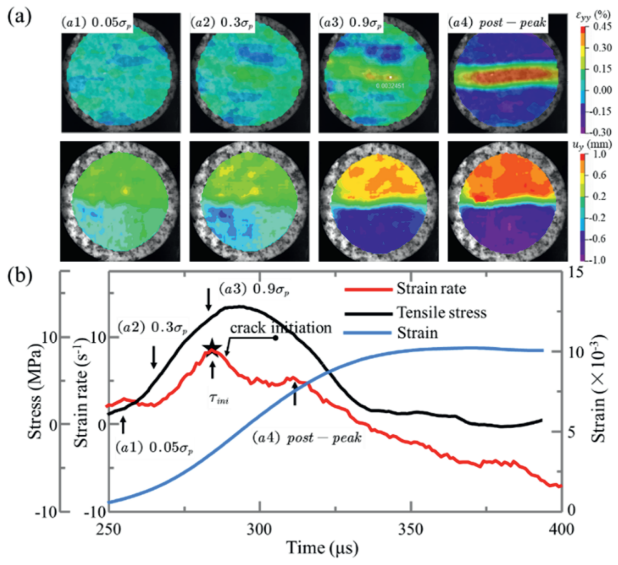

Fig. 8. (a) The experimental displacement fields at different stress levels, (b) history curves of the tensile stress, strain rate and strain distribution of sample GB-3-5.6.

results in evident COD at that instant. That implies that the drop of stress is a result of a boundary failure rather than the fracturing of the centreline.

Based on the evolution of strain fields estimated by DIC analysis, the relations between the crack initiation, peak failure and boundary failure can be investigated and compared. As discussed above, the critical moment of boundary failure on horizontal deformation is not significant. The value of ε_{xx} generally increases as the loading is continued. The time interval between two lines is 5 μs, and the moment when the peak stress occurs is 295 μs. In Fig. 9a, the average value of ε_{yy} corresponding to crack initiation is 0.32 %. The value of boundary failure is 1.0 % in post-peak, and after that moment, the strain field is dramatically distributed because of the displacement discontinuity.

We obtained stress-strain curves using DIC analysis, as shown in Fig. 10. The tensile strain at the centre of the disc rapidly increases and results in great errors in the post-peak stage. The strain rate of the virtual DIC strain gauge shows a dramatic increase compared with that of the physical strain gauge. The strain rate corresponding to crack initiation is 5.3 s^{-1} from the strain gauge and 13.8 s^{-1} from DIC measurement. The peak strain rate from the strain gauge is 13.6 s^{-1}, which is much smaller than that value on the curve of $\dot{\varepsilon}_{DIC}$ (~40 s^{-1}). The actual increase of tensile strain rate is the red dotted line presented in Fig. 10b; the critical point is the moment that the sample reaches its peak stress. After this moment, the stress starts to drop while the strain is still

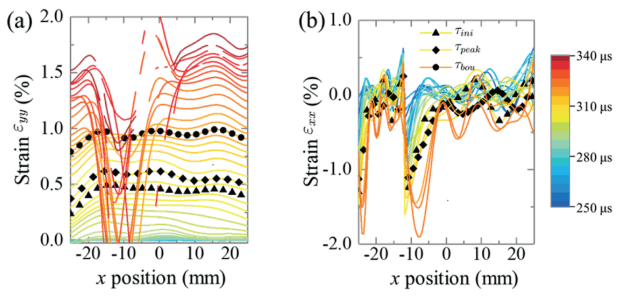

Fig. 9. (a) The experimental vertical strain and (b) the horizontal strain on the centreline at different moments, the lines with dots are the moments corresponding to crack initiation, peak stress and boundary failure, respectively.

increasing. Therefore, that means the actual strain and strain rate of the sample in the post-peak can only be obtained from the direct measurement, such as a strain gauge on the sample or DIC approach.

3.5. Crack initiation and propagation

The crack initiation and propagation should be evaluated to understand whether the failure is (a) initiated from the centre of the disc and (b) whether the crack path is symmetric. Three strain gauges are mounted on the back of the rock sample. The arrangement of the strain gauges (abbreviated sg) is as follows:

(1) sg.1 is located along the centreline at 10 mm away from the end of the incident bar
(2) sg.2 is mouthed at the middle of the sample and
(3) sg.3 is 15 mm away from sg.2.

Fig. 11a and b shows typical dynamic results of sample GB-1-4.5. The electric voltages of sg.1 and sg.2 dramatically increase when the incident wave reaches the sample, and the step-like onsets mean that the strain gauges are broken. However, sg.3 increases slowly after crack initiation because the main crack fails to cross the strain gauge. The loss of the simultaneous increase in sg.1 and sg.3 reveals that the crack propagation in the sample is asymmetric. The onset of sg.2 corresponds to the moment of 50 % peak stress. By defining the point where the voltage signal dramatically increases as the crack initiation point, the cracking time of sg.2 is $\tau^1_{ini} = 432$ μs and the corresponding values for sg.3 and sg.1 are 462 μs and 457 μs, respectively. The mean crack velocity can be estimated by $\frac{\Delta L}{\Delta \tau}$, and the value is 500 m/s herein.

Estimation of crack velocity using strain gauges is limited to the accurate location of crack tips (Ju et al., 2019). The results from the strain gauge will be valid only when the crack propagates through it. DIC has been proven as an effective method to determine the fracturing process and propagation for rocks (Ju et al., 2019). From the results presented in Fig. 12, the evolution of displacement, strain and fracturing sequence can be acquired by DIC. Only u_y and ε_{yy} are illustrated here because the vertical variables are more sensitive to the displacement discontinuity. From the profiles of vertical displacement, the crack initiates at the centre of the disc with a maximum displacement step of 0.9 mm when the stress level is 0.9 σ_p. The tip of the discontinuity propagates to the ends of the sample, and the maximum tensile strain is approximately 1.0 % when the stress reaches its peak value. Accordingly, the displacement step is 1.5 mm. The location of the crack tips can be found by defining the critical tension strain: in this study, the tensile strain threshold is 0.32 %. Hence, the evolution of crack tips in association with time is indicated by the arrows on the profiles of strain, while the white arrows denote the crack tips labelled from visual analysis of the images. Fig. 13a presents the COD of seven virtual gauges located on the centreline. It's noted that line (1) firstly increases at a time of 250 μs, shortly followed by lines (2) and (3). The displacement gradients are calculated to identify the position of transit tips of the crack, and the results of crack velocity are plotted in Fig. 13b. As mentioned previously, the mean crack velocity determined by strain gauges is 500 m/s, which significantly overestimates the crack velocity, as we treated the beginning points of step-like voltage as the crack initiation moment. From the results estimated by visual observation, it is difficult to precisely capture crack tips and, therefore, the crack velocity is generally underestimated. The DIC method provides the real-time change of the crack velocity as well as the propagation direction. The value of the crack velocity experimentally determined by DIC

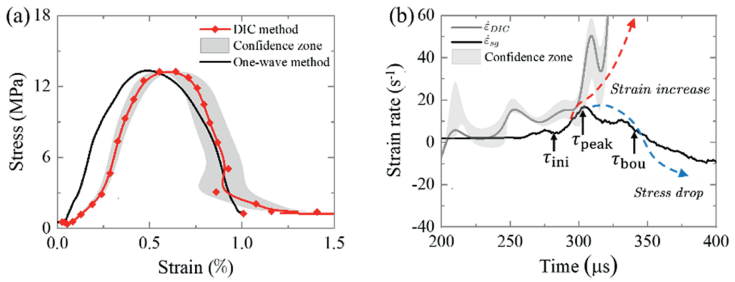

Fig. 10. (a) The stress-strain curves computed by DIC analysis and the strain gauge method. (b) Comparison of strain rates computed by the strain gauge method and DIC method.

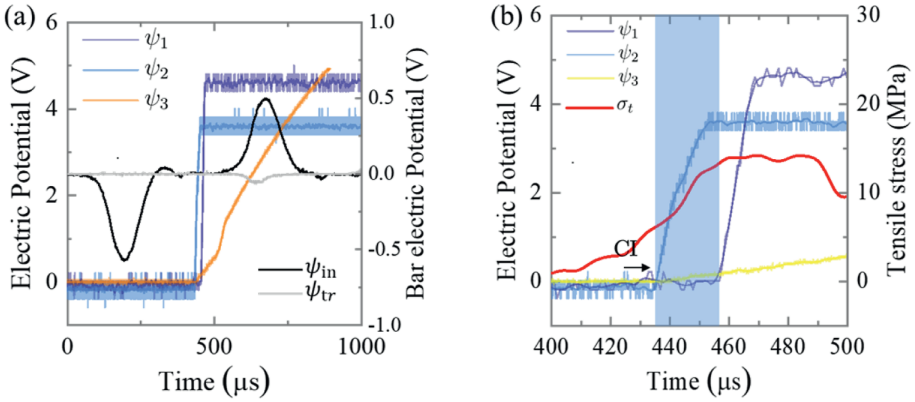

Fig. 11. (a) Dynamic results of the typical sample GB-1-4.5, and (b) history of tensile stress after shifting the transmitted wave.

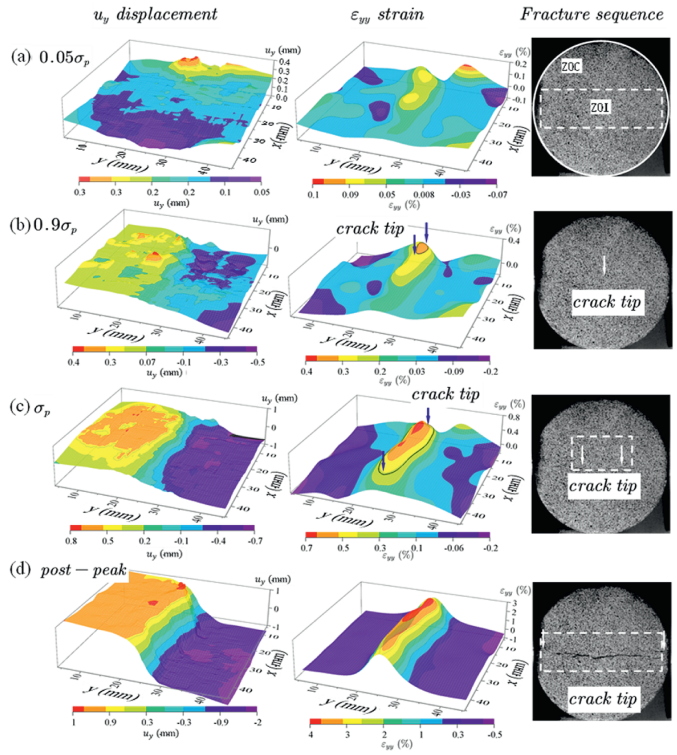

Fig. 12. Fracturing sequence, vertical displacement and strain fields recorded by high-speed camera for rock sample GB-3-5.6, the first column shows the displacements in *y*-direction, and the second column shows the DIC results of strain ε_{yy}, the third column shows images of the fracturing process.

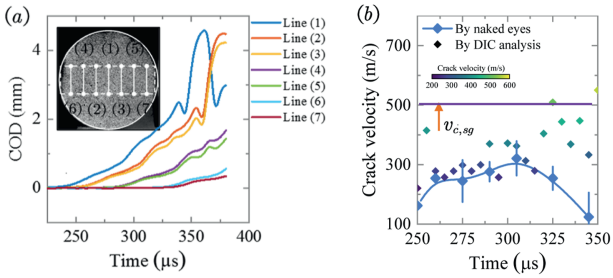

Fig. 13. (a) The location of the virtual gauges and COD as a function of time, (b) the comparison of crack velocity computed from DIC, strain gauge and visual method.

is between 200 m/s to 600 m/s. This value is slightly increased when the crack approaches the ends of the sample. Besides, the crack velocity propagating in the left part of the disc is larger than that in the right part, which means the crack propagation is asymmetric.

4. Discussion

4.1. Rate dependency of tensile strength

Understanding the mechanism of rate-dependency is crucial to investigating the fracturing and fragmentation of brittle materials subject to impact load (Grady and Lipkin, 1980; Li et al., 2018a). Li et al., (2018b) summarised the dynamic strength models of geo-materials under uniaxial compression state and proposed a unified form of the DIF as a function of strain rate

$$\frac{\sigma_d}{\sigma_\tau} = 1 + \left(\frac{\dot{\varepsilon}}{\dot{\varepsilon}_s}\right)^{\beta} \tag{12}$$

where σ_τ is the quasi-static tensile strength, $\dot{\varepsilon}_s$ and β are dynamic parameters depending on material properties. For arbitrary β, the DIF is 2.0 when the strain rate equals the characteristic strain rate $\dot{\varepsilon}_s$. β is the dynamic increase factor only determined from initial defects within the sample.

Table 2 lists the theoretical results of the dynamic increase factor for different rocks. Grady and Hollenbach (1979) conducted plate impacts on oil shales and suggested the dynamic increase factor is 0.33 and 0.25 when the strain rate is 10^4 s^{-1}. The dynamic increase factor for Limestone is valued as 0.05 by Lipkin and Jones (1979) and as 0.19 by Grady and Lipkin (1980). Kimberley et al. (2013) assume the dynamic increase factor to be the same for all brittle materials, equal to 0.67. Li et al., (2018b) summarised the dynamic behaviour of different rock types and found that the value of the dynamic increase factor is influenced by the rock types, but always in between 0.31 and 0.79.

Kimberley et al. (2013) proposed the upper-bound solution of the characteristic strain rate when the crack velocity approaches to Rayleigh wave velocity as $\dot{\varepsilon}_s = \alpha v_c K_{IC} \eta^{1/4}/(\bar{s}E)$, where v_c is the Rayleigh wave velocity; K_{IC} is the mode I fracture toughness (Pa $m^{1/2}$); $\bar{s}$ is the mean defect size (m); η is the crack area density (m^{-2}); and α is a dimensionless material parameter.

From the increase tendency of DIF predicted by Eq. (12) and experiment results in Fig. 1, the rate dependency of tensile strength can be divided into three regions: (a) region I (<1 s^{-1}) is rate independent; (b) region II (1-30 s^{-1}) is the range conducted by SHPB apparatus, the DIF increases from 1.0 to 7.0 and the materials behave evident increasing tendency as the strain rate increases in this range; and (c) region III^b (>30 s^{-1}) violates the increasing tendency predicted by theoretical model, the DIF decreases when the strain rate exceeds a certain threshold value.

Table 3 illustrates experimental results of granites under different strain rates. $\dot{\varepsilon}_{sg}$ is the strain rate computed from the strain gauge, and $\dot{\varepsilon}_{DIC}$ is that value directly obtained from DIC analysis.

The stress-strain curves and the dynamic increase factor as a function of strain rate are plotted in Fig. 14. As described above, the variation of peak stress with strain rate is not strictly coincident. Due to the limitation of the SHPB apparatus, it is hard to obtain the failure strength in region I, which is illustrated in Fig. 1a. The tensile strength in region II is significantly dependent on the strain rate. For the granite used in this study, the DIF ranges from 1.3 to 2.7. The discrepancy in tensile strength shows that the DIF decreases with the increase of strain rate in region III^b. The strain rate measured from the strain gauge was in the range of 5.1–65 s^{-1}, whereas the DIC result ranged from 17 s^{-1} to 213 s^{-1}. As illustrated in Fig. 14b and c, the dot lines represent results obtained by strain gauge and DIC analysis, which exclude the invalid results in region III^b, and the predicted characteristic strain rates are 14.5 s^{-1} and 48.3 s^{-1}, respectively. But the corresponding characteristic strain rates of the results, including region III^b are 48.8 s^{-1} and 141 s^{-1}, and the dynamic increase coefficients are 0.14 and 0.15, respectively. The β shows the rate dependency of the tensile strength on strain rate, that value commonly ranges from 0.31 to 0.79 in compression tests for different rocks (Li et al., 2018b). The theoretical strain rate can be estimated by $\dot{\varepsilon}_s = \frac{\alpha v_c K_{IC} \eta^{\frac{1}{4}}}{(\bar{s}E)}$, Rayleigh wave velocity c_R in this study is 2562 m/s. Assuming the average defect size of the specimen to be $\bar{s}$ = 1 mm, the defect spacing l_η = 2.0–3.5 mm and the fracture toughness K_{IC} = 1.6 MPa $m^{1/2}$, the density of crack area is $\eta = 0.82 \times 10^6$ m^{-2}. α is the parameter related to material strength, which meets $\alpha = \sigma_t \bar{s} \eta^{1/4}/K_{IC}$, α can be set as 0.21 for tension tests. It is worth noting that the actual crack velocity is much slower than the Rayleigh wave and, in this study, it ranges from 200 m/s to 600 m/s. Therefore, the theoretical characteristic strain rate should be in the range of 12–62 s^{-1}. However, the characteristic strain rates, including region III^b, exceed the upper bound of the theoretical prediction, while those values, excluding region III^b, are between 14.5 s^{-1} and 48.3 s^{-1}, thus more consistent with the theoretical solution. By using DIC analysis, the characteristic strain rate is 48.3 s^{-1}, the dynamic increase factor is 0.97, and the coefficient of determination is $R^2 = 0.88$. Thus, the unified dynamic increase factor model of Eq. (12) well predicts the dynamic behaviour of rocks as well as the characteristic strain rate.

$$\left.\begin{aligned} \frac{\sigma_{td}}{\sigma_\tau} &= 1 + \left(\frac{\dot{\varepsilon}_{sg}}{48.5}\right)^{0.14}, \ R^2 = 0.28 \\ \frac{\sigma_{td}}{\sigma_\tau} &= 1 + \left(\frac{\dot{\varepsilon}_{DIC}}{141}\right)^{0.15}, \ R^2 = 0.28 \end{aligned}\right\} \text{Including region III}^b \tag{13}$$

$$\left.\begin{aligned} \frac{\sigma_{td}}{\sigma_\tau} &= 1 + \left(\frac{\dot{\varepsilon}_{sg}}{14.5}\right)^{0.94}, \ R^2 = 0.82 \\ \frac{\sigma_{td}}{\sigma_\tau} &= 1 + \left(\frac{\dot{\varepsilon}_{DIC}}{48.3}\right)^{0.97}, \ R^2 = 0.88 \end{aligned}\right\} \text{Excluding region III}^b \tag{14}$$

4.2. The determination on CVSr

As depicted in section 4.1, the relation between the tensile strength and strain rate can be divided into regions I, II and III. In region III, the increase in tensile strength with strain rate is no longer observed. Fig. 15 shows four typical results of the stress equilibrium factor under different strain rates. The stress equilibrium factor below −5 % is the loading stage from t = 50–150 μs. When it falls within 5 %, the equilibrium is achieved and can be regarded as the boundary between the unbalanced and balanced

Table 2
The theoretical results of the dynamic increase factor of brittle materials.

Material	Methodology	Dynamic increase factor	Reference
Arkansas Novaculite	Plate impact	1/3	Grady and Kipp (1979)
Quartz Monzonite	SHPB test	1/3	Birkimer (1970)
Westerly Granite	SHPB test	1/3	Lipkin et al. (1977)
Solenhofen Limestone	SHPB test	0.05	Lipkin et al. (1977)
Oakhall Limestone	SHPB test	0.19	Lipkin et al. (1977)
	Taylor plate	0.25	Grady and Hollenbach (1979)
Oil Shale	Electromagnetic shock	1/3	
	SHPB test	–	Lipkin and Jones (1979)
Concrete	SHPB test	1/3	Birkimer (1970)

Table 3
Brazilian disc experimental results of granites.

Sample No.	v_s (m/s)	d_s (mm)	b_s (mm)	$\dot{\varepsilon}_{sg}$ (s^{-1})	$\dot{\varepsilon}_{DIC}$ (s^{-1})	σ_t (MPa)	Boundary failure condition
GBs-0	–	49.8	24.5	1e-5	–	11.2	Intact, type I
GB-1-4.5	4.5	49.6	24.8	6.24	24.5	15.4	Intact, type I
GB-2-4.8	4.8	48.3	25.1	5.1	17	14.5	Intact, type I
GB-3-5.6	5.6	49.2	25.2	13.6	47	16.3	Split, conical failure, type I
GB-4-7.1	7.1	51.3	24.9	16.4	68.4	29.2	Split, conical failure, type II
GB-5-7.6	7.6	49.3	24.7	26.3	75.4	23.4	Split, fails to capture
GB-6-6.7	6.7	50.1	25	14.81	42.6	19.7	Right end failure
GB-7-8.1	8.1	49.4	24.8	18.6	64.8	23.3	Split, fragmented, type II
GB-8-8.7	8.7	50.2	24.6	21.3	54.6	31.0	Split, crack branch, type II
GB-9-7.9	7.9	50.6	25.2	54.3	164	22.2	Fragmented, type IV
GB-10-8.9	8.9	49.1	25.1	58.4	154	22.1	Split, crack branch, type IV
GB-11-9.2	9.2	49.8	25.3	64.3	184	18.6	Split, conical failure, type III
GB-12-9.7	9.7	49.4	25.2	77.6	213	24.6	Left end failure, type III
GB-13-10.6	10.6	49.7	25.0	38.5	121.3	18.4	Left end fragmented, type III

Note: type I failure is an ideal failure mode, indicating the crack initiates from the centre of the disc; type II failure is dominated by tensile cracks on the centreline with forming obvious pressurised zones; type III failure is induced by the failure of loading boundary at the end of the transmitted rod and type IV failure is induced by unbalanced loading.

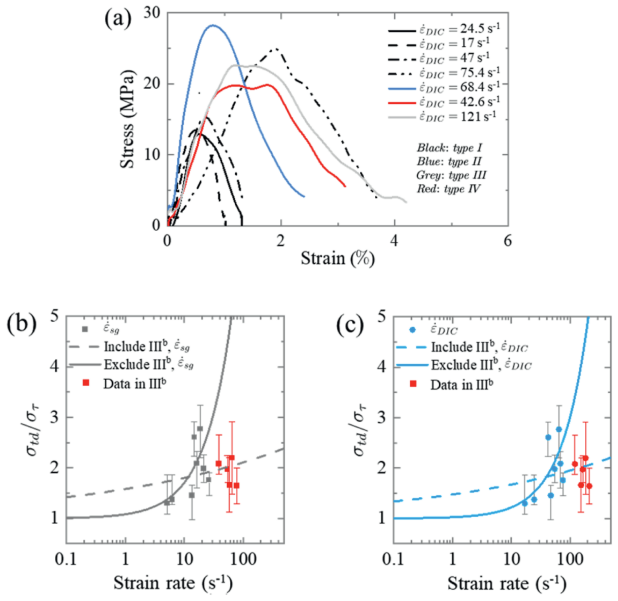

Fig. 14. The stress-strain curves and tensile strengths as a function of strain rate, (a) stress-strain curves and (b) the dependency of tensile strength on strain rate.

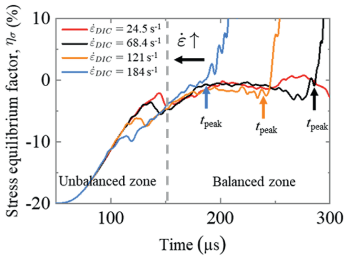

Fig. 15. History curves of the stress equilibrium factor under different strain rates.

zone. The result reveals that less time will be consumed to get the stress equilibrium at the lower loading rate, meaning that it is easier to obtain the valid tensile strength in BD tests. The stress wave already travels several rounds in the sample to realise an equilibrium state before the balance stage. If the moment of peak stress falls out of the balanced zone, which means the failure occurs when the moment is in an unbalanced state, which violates the validity of SHPB tests.

From the experimental results, the failure modes of the dynamic splitting test can be divided into four types, as shown in Fig. 16. Type I is an ideal failure mode, indicating the crack initiates from the centre of the disc. The shear cracks at the interface sample bars are few and do not influence the distribution of tensile stress along the centreline. This failure type was only observed in quasi-static test and in samples of GB-1, GB-2 and GB-3 with a strain rate less than 24.5 s^{-1}. Type II is a common failure mode dominated by tensile cracks on the centreline with forming obvious pressurised zones at both ends of the sample. Under certain circumstances, crack bifurcation may occur and result in debris around the centreline. The shear crush beneath the loading points may occur after a tensile crack has already initiated at the centre of the disc, therefore it does not break the assumption of the dynamic BD test. This mode was found in samples GB-3-5.6 and GB-4-7.1, and the maximum strain is 68.4 s^{-1}. The appearance of type III is induced by the failure of loading boundary at the end of the transmitted rod. This failure may be caused by reflected tensile waves resulting from poor initial contact or unevenness of the end of the sample. This situation causes stress differences during loading and results in invalid testing results. Type IV is a common failure mode for unbalanced loading. When the strain rates reach a certain threshold level, the stress difference during the balancing process is sufficient to cause pressurised damage at the end of the incident rod, which directly leads to instability of the boundary.

The non-uniform stress distribution and coupled stress state increase the complexity of the fracture criterion. The recommended strain rate operated by conventional SHPB is on the order of 10 s^{-1} to 10^4 s^{-1} (Kolsky, 1949). Recently, Staehler et al. (1993) have reported a discrepancy in material behaviour beyond the CVSr. The results indicate that for tests above 2700 s^{-1}, the compressive stress will be 50 % lower. Many other researchers (Ravichandran and Subhash, 1994; Jia and Ramesh, 2004; Pan et al., 2005) also reported that there is an upper limit of the achievable strain rate in brittle materials using SHPB. Assuming the rock is linearly elastic until failure, the average strain rate in the sample can be calculated as

$$\dot{\varepsilon}_{\lim,1} = \frac{\varepsilon_r}{\tau} \tag{15}$$

where ε_r is the rupturing strain of the material under tensile stress, which is taken as 0.32 % in this study. The failure time τ should never be less than the time to reach the balanced state. Generally,

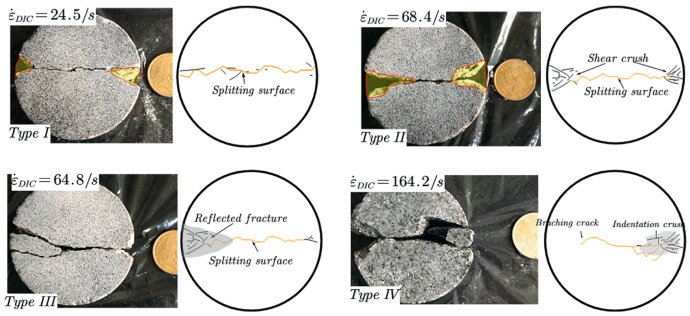

Fig. 16. The fundamental failure modes in the Brazilian disc test subject to impact loads.

the loading stress wave will travel 5–10 rounds to realise stress equilibrium in the specimen. Hence, the CVSr can be estimated by $\dot{\varepsilon}_{\mathrm{lim},1} = \frac{c\varepsilon_r}{10r}$, in which c is the P-wave velocity, and the theoretical value of CVSr is $\dot{\varepsilon}_{\mathrm{lim},1} = 76\ \mathrm{s}^{-1}$. This value only considers the stress equilibrium hypothesis before the failure. For the BD test, the assumption of crack initiation from the centreline will be broken when the fracture initiates from the loading boundary. If we assume the end of the sample to be a point contact by a disc with radius r, the maximum tensile stress at the circular boundary can be calculated according to the Hertzian contact theory as

$$\sigma_{\mathrm{t}} = \frac{(1-2\upsilon)P}{2\pi a^2} \tag{16}$$

where a is the radius of the contact surface as shown in Fig. 17a. σ_{t} is the tensile stress induced by Hertzian indentation, and the tensile failure occurs when it equals the tensile strength $\hat{\sigma}_{\mathrm{t}}$ of the rock. Assume the boundary will be destroyed when the crack under the contact point propagates to a distance of a. The time before the loading wave reaches the right end of the sample is $t_{\mathrm{f}} = a/v_{\mathrm{crack}}$. Therefore, the CVSr determining the central crack initiation is obtained by substituting Eq. (2) into Eq. (16)

$$\dot{\varepsilon}_{\mathrm{lim},2} = \frac{\varepsilon_{\mathrm{r}} a v_{\mathrm{crack}}}{(1-2\upsilon)b_{\mathrm{s}} r} = \lambda \frac{\varepsilon_{\mathrm{r}} v_{\mathrm{crack}}}{(1-2\upsilon)b_{\mathrm{s}}} \tag{17}$$

where v_{crack} is the crack velocity. It is noted that $\dot{\varepsilon}_{\mathrm{lim},2}$ is dependent on the ratio of a to radius r, the failure beneath the ends of the sample will disturb the stress field in the specimen, and break the requirement of central crack initiation as the failure range λ is large enough. Fig. 17b shows the CVSr as a function of sample radius. It should be noted that the critical strain rate $\dot{\varepsilon}_{\mathrm{lim},2}$ in Eq. (17) is determined by λ rather than the radius of the sample. The upper strain rate of $\dot{\varepsilon}_{\mathrm{lim},1}$ decreases with the increase of sample radius, but the CVSr is codetermined by $\dot{\varepsilon}_{\mathrm{lim},1}$ and $\dot{\varepsilon}_{\mathrm{lim},2}$. When the length ratio λ increases from 0.001 to 0.5, the upper critical strain rate of $\dot{\varepsilon}_{\mathrm{lim},2}$ increases. The CVSr will be determined by $\dot{\varepsilon}_{\mathrm{lim},2}$ if the length ratio is small.

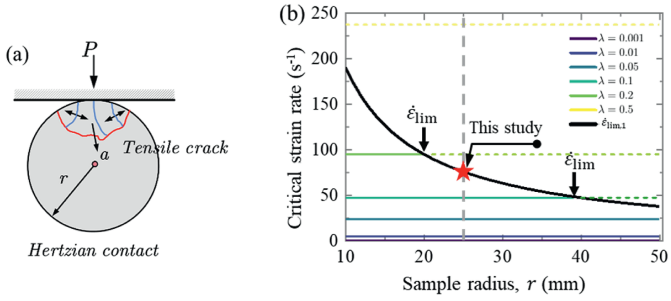

Fig. 17. (a) Schematic diagram of the point contact between the sample and rod. (b) CVSr range dominated by stress equilibrium and central crack initiation.

In fact, the existence of a crushed zone under the loading points has little influence on the maximum principal stress distribution in the centre of the disc if the crack length is less than $0.2r$. Therefore, for the sample radius of 25 mm used in this study, the theoretical CVSr result is close to 75 s^{-1}. This value is very close to the measured maximum strain rate by DIC analysis for type I and type II, which is 68.4 s^{-1} in this study.

The CVSr can be roughly estimated from the equations discussed above. It was found that the critical strain rate is mainly influenced by the sample radius. Due to the heterogeneity of rocks and the suggested size by ISRM, the available sample size can be chosen for the BD test is very limited. Unfortunately, it is still unknown whether this critical strain rate is dependent on the rock type. It appears that the range of CVSr is influenced to some extent because the fracture strain and wave velocity are different for different rocks. However, it is also clear from the results in Fig. 1b that rock type does not affect the value of CVSr as expected.

Overall, the assessment of the validity of the stress state is an indispensable procedure of the dynamic splitting test. The evaluation should be carried out by the three-wave method, stress equilibrium factor and the failure patterns recommended in this study. The reliability of over-strain rate data in previous experiments deserves further discussion. Of course, adopting the modified Brazilian splitting method, such as the flattened BD test (Wang et al., 2006) and the BD test with jaws (Dai et al., 2010a) can reduce the uncertainty of the traditional BD method. But for higher strain rate testing of rocks in tension, some direct methods, such as the spalling test or Taylor impact, are recommended to avoid the uncertainty associated with the BD test.

4.3. Limitations

The CVSr in dynamic Brazilian disc tests is defined by requiring the peak strain to occur after stress equilibrium. However, the wave travel distance required for stress balance can only be determined empirically and roughly in a range of 5–10 rounds. Because this distance is determined by a complex interaction of multiple factors, e.g. diameter/thickness ratio, wave impedance mismatch between specimen and bar, loading pulse characteristics and so on. These complexities introduce uncertainty to CVSr value. Furthermore, the CVSr value might change when employed in other rock types, as wave velocity might differ. This highlights the need for the development of a universal CVSr model in the future.

In addition, due to resource constraints, this study is solely restricted to granite. While the four failure modes identified in this study should be theoretically applicable to other brittle rocks (given granite's representative behaviour), ductile rocks (e.g.

halite, gypsum, and mudstone) may exhibit fundamentally different responses under dynamic BD testing, warranting future investigation.

5. Conclusions

In this study, BD tests are performed on granitic rocks in combination with DIC and SHPB setup. We performed a comparison between the strain gauge measurements with DIC results to ensure the validity of DIC analysis. Then, the evolutions of displacement and strain fields are explored to present the spatial and temporal changes of deformation under different strain rates. The actual deformation and strain rate are much larger than those measured from conventional strain gauges, which are limited to boundary continuity. Finally, the rate dependency of tensile strength for rocks is discussed to calibrate the unified DIF model. The validity of the loading condition, based on the CVSr determined by the required conditions of stress equilibrium and central crack initiation, is investigated. The main conclusions are:

(1) The tensile strength of granite is significantly dependent on strain rate. There are three regions in the experimental results of DIF as a function of strain rate. The discrepancy in region III is a result of boundary failure and violates the validity of the dynamic BD test. The unified DIF model is extended to tension tests after eliminating abnormal results. The calculated characteristic strain rate is 48.3 s^{-1}, which agrees more with the theoretical prediction range (12-62 s^{-1}).
(2) The values of strain and strain rate experimentally measured by DIC are larger than those from strain gauges. Because the strain measured from strain gauges is an average value on the centreline, the strain in the post-peak stage is not the actual deformation of the sample due to the separation between the sample and rods. DIC can overcome these shortcomings and estimates the actual value of tensile strain for crack initiation to be 0.32 %, and the crack velocity to range from 200 m/s to 600 m/s.
(3) The theoretical CVSr, co-determined by stress equilibrium and boundary failure, is 75 s^{-1}. This value matches well with the measured CVSr ($\dot{\varepsilon} = \frac{68.4}{s}$) from DIC measurements. With the increase in strain rate, the failure pattern of rocks can be categorised into four types: splitting → splitting and fracturing → asymmetric fracturing → boundary failure. The appearance of boundary failure, e.g. type III and IV, indicates that the assumptions at the base of the BD test are not met, meaning that the validity of experiments is broken as the strain rate reaches a certain level. The influence of rock types on CVSr is unknown, and it should be studied in the future.

CRediT authorship contribution statement

Xiaofeng Li: Writing – review & editing, Writing – original draft, Visualization, Resources, Methodology. **Haibo Li:** Writing – review & editing, Investigation, Funding acquisition. **Giovanni Grasselli:** Investigation, Funding acquisition.

Declaration of competing interest

The authors declare that they have no known competing financial interests or personal relationships that could have appeared to influence the work reported in this paper.

Acknowledgments

The editorial advice and suggestions from anonymous reviewers are acknowledged. We would like to thank Prof. Jian Zhao of Monash University for extensive discussions of this manuscript. This work was supported by the Natural Sciences and Engineering Research Council of Canada (NSERC) Discovery Grants 341275, and Katia Ossetchkina from University of Toronto is specially acknowledged for her kind help to improve the manuscript.

References

Albertini, C., Montagnani, M., 1994. Study of the true tensile stress-strain diagram of plain concrete with real size aggregate; need for and design of a large Hopkinson bar bundle. J. Phys. IV 4, C8–C113.
Asprone, D., Cadoni, E., Prota, A., Manfredi, G., 2009. Dynamic behavior of a Mediterranean natural stone under tensile loading. Int. J. Rock Mech. Min. Sci. 46, 514–520.
Birkimer, D.L., 1970. A possible fracture criterion for the dynamic tensile strength of rock. In: U.S. Rock Mechanics/Geomechanics Symposium. P. ARMA-70-0573.
Cadoni, E., 2010. Dynamic characterization of orthogneiss rock subjected to intermediate and high strain rates in tension. Rock Mech. Rock Eng. 43, 667–676.
Cai, M., Kaiser, P.K., Tasaka, Y., Minami, M., 2007. Determination of residual strength parameters of jointed rock masses using the GSI system. Int. J. Rock Mech. Min. Sci. 44, 247–265.
Cai, M., Kaiser, P.K., Duff, D.J., 2012. Rock support design in burst-prone ground utilizing an interactive design tool. In: 46th US Symposium Rock Mechanics/Geomechanics Chicago2012, pp. 2024–2032.
Chen, R., Dai, F., Qin, J., Lu, F., 2013. Flattened Brazilian disc method for determining the dynamic tensile stress-strain curve of low strength brittle solids. Exp. Mech. 53, 1153–1159.
Chen, J.J., Guo, B.Q., Liu, H.B., Liu, H., Chen, P.W., 2014. Dynamic Brazilian Test of brittle materials using the split hopkinson pressure bar and digital image correlation. Strain 50, 563–570.
Cho, S.H., Ogata, Y., Kaneko, K., 2003. Strain-rate dependency of the dynamic tensile strength of rock. Int. J. Rock Mech. Min. Sci. 40, 763–777.
Dai, F., Xia, K., 2010. Loading rate dependence of tensile strength anisotropy of Barre granite. Pure Appl. Geophys. 167, 1419–1432.
Dai, F., Huang, S., Xia, K., Tan, Z., 2010a. Some fundamental issues in dynamic compression and tension tests of rocks using split Hopkinson pressure bar. Rock Mech. Rock Eng. 43, 657–666.
Dai, F., Xia, K., Tang, L., 2010b. Rate dependence of the flexural tensile strength of Laurentian granite. Int. J. Rock Mech. Min. Sci. 47, 469–475.
Dutta, P.K., Kim, K., 1993. High-Strain-Rate Tensile Behavior of Sedimentary and Igneous Rocks at Low Temperatures.
Field, J.E., Walley, S.M., Proud, W.G., Goldrein, H.T., Siviour, C.R., 2004. Review of experimental techniques for high rate deformation and shock studies. Int. J. Impact Eng. 30, 725–775.
Fourmeau, M., Gomon, D., Vacher, R., Hokka, M., Kane, A., Kuokkala, V.-T., 2014. Application of DIC technique for studies of kuru granite rock under static and dynamic loading. Procedia Mater. Sci. 3, 691–697.
Gao, G., Huang, S., Xia, K., Li, Z., 2015. Application of Digital Image Correlation (DIC) in dynamic notched semi-circular Bend (NSCB) tests. Exp. Mech. 55, 95–104.
Goldsmith, W., Sackman, J.L., Ewerts, C., 1976. Static and dynamic fracture strength of Barre granite. Int. J. Rock Mech. Min. Sci. 13, 303–309.
Gomez, J., Shukla, A., Sharma, A., 2001. Static and dynamic behavior of concrete and granite in tension with damage. Theor. Appl. Fract. Mech. 36, 37–49.
Grady, D.E., Hollenbach, R.E., 1979. Dynamic fracture strength of rock. Geophys. Res. Lett. 6, 73–76.
Grady, D.E., Kipp, M.E., 1979. Oil shale fracture and fragmentation at higher rates of loading. In: U.S. Rock Mechanics/Geomechanics Symposium. P. ARMA-79-0403.
Grady, D.E., Kipp, M.E., 1980. Continuum modelling of explosive fracture in oil shale. Int. J. Rock Mech. Min. Sci. Geomech. Abstr. 17, 147–157.
Grady, D.E., Lipkin, J., 1980. Criteria for impulsive rock fracture. Geophys. Res. Lett. 7, 255–258.
Griffith, W.A., St Julien, R.C., Ghaffari, H.O., Barber, T.J., 2018. A tensile origin for fault rock pulverization. J. Geophys. Res. Solid Earth 123, 7055–7073.
Heard, W., Song, B., Williams, B., Martin, B., Sparks, P., Nie, X., 2018. Dynamic tensile experimental techniques for geomaterials: a comprehensive review. J. Dyn. Behav. Mater. 4, 74–94.
Hogan, J.D., Kimberley, J., Hazeli, K., Plescia, J., Ramesh, K.T., 2015. Dynamic behavior of an ordinary chondrite: the effects of microstructure on strength, failure and fragmentation. Icarus 260, 308–319.
Howe, S.P., Goldsmith, W., Sackman, J.L., 1974. Macroscopic static and dynamic mechanical properties of Yule marble - the mechanical properties of a commercially purchased slab of Yule marble are investigated primarily as a function of strain rate, without consideration of the effects of other paramete. Exp. Mech. 14, 337–346.
Huang, S., Chen, R., Xia, K.W., 2010a. Quantification of dynamic tensile parameters of rocks using a modified Kolsky tension bar apparatus. J. Rock Mech. Geotech.

Eng. 2, 162–168.
Huang, S., Xia, K., Yan, F., Feng, X., 2010b. An experimental Study of the rate dependence of tensile strength softening of Longyou sandstone. Rock Mech. Rock Eng. 43, 677–683.
Huang, J., Xu, S., Yi, H., Hu, S., 2014. Size effect on the compression breakage strengths of glass particles. Powder Technol. 268, 86–94.
Jia, D., Ramesh, K.T., 2004. A rigorous assessment of the benefits of miniaturization in the Kolsky bar system. Exp. Mech. 44, 445–454.
Jones, E.M.C., Iadicola, M.A., 2018. A good practices guide for digital image correlation. Int. Digit. Image Correl. Soc 10, 308–312.
Ju, M., Li, J., Yao, Q., Li, X., Zhao, J., 2019. Rate effect on crack propagation measurement results with crack propagation gauge, digital image correlation, and visual methods. Eng. Fract. Mech. 219, 106537.
Khan, A.S., Irani, F.K., 1987. An experimental study of stress wave transmission at a metallic-rock interface and dynamic tensile failure of sandstone, limestone, and granite. Mech. Mater. 6, 285–292.
Kimberley, J., Ramesh, K.T., Daphalapurkar, N.P., 2013. A scaling law for the dynamic strength of brittle solids. Acta Mater. 61, 3509–3521.
Klepaczko, J.R., Brara, A., 2001. An experimental method for dynamic tensile testing of concrete by spalling. Int. J. Impact Eng. 25, 387–409.
Kolsky, H., 1949. An investigation of the mechanical properties of materials at very high rates of loading. Proc. Phys. Soc. B 62, 676–700.
Kubota, S., Ogata, Y., Wada, Y., Simangunsong, G., Shimada, H., Matsui, K., 2008. Estimation of dynamic tensile strength of sandstone. Int. J. Rock Mech. Min. Sci. 45, 397–406.
Li, Y., Ramesh, K.T., 2007. An optical technique for measurement of material properties in the tension Kolsky bar. Int. J. Impact Eng. 34, 784–798.
Li, X.F., Li, H.B., Zhang, Q.B., Jiang, J.L., Zhao, J., 2018a. Dynamic fragmentation of rock material: characteristic size, fragment distribution and pulverization law. Eng. Fract. Mech. 199, 739–759.
Li, X.F., Zhang, Q.B., Li, H.B., Zhao, J., 2018b. Grain-Based discrete element method (GB-DEM) modelling of multi-scale fracturing in rocks under dynamic loading. Rock Mech. Rock Eng. 51, 3785–3817.
Li, X.F., Li, H.B., Zhao, J., 2021. Transgranular fracturing of crystalline rocks and its influence on rock strengths: insights from a grain-scale continuum–discontinuum approach. Comput. Methods Appl. Mech. Eng. 373, 113462.
Lipkin, J., Grady, D.E., Campbell, J.D., 1977. Dynamic flow and fracture of rock in pure shear. In: U.S. Rock Mechanics/Geomechanics Symposium. P. ARMA-77-0180.
Lipkin, J., Jones, A.K., 1979. Dynamic fracture strength of oil shale under torsional loading. In: ARMA US Rock Mechanics/Geomechanics Symposium, pp. ARMA–79.
Pan, Y., Chen, W., Song, B., 2005. Upper limit of constant strain rates in a split Hopkinson pressure bar experiment with elastic specimens. Exp. Mech. 45, 440–446.
Pan, B., Lu, Z., Xie, H., 2010. Mean intensity gradient: an effective global parameter for quality assessment of the speckle patterns used in digital image correlation. Opt Laser. Eng. 48, 469–477.
Peters, W.H., Ranson, W.F., 1982. Digital imaging techniques in experimental stress analysis. Opt. Eng. 21, 213427.
Pierron, F., Sutton, M.A., Tiwari, V., 2011. Ultra high speed DIC and virtual fields method analysis of a three point bending impact Test on an aluminium bar. Exp. Mech. 51, 537–563.
Ravichandran, G., Subhash, G., 1994. Critical appraisal of limiting strain rates for compression testing of ceramics in a split hopkinson pressure bar. J. Am. Ceram. Soc. 77, 263–267.
Saksala, T., Hokka, M., Kuokkala, V.-T., Mäkinen, J., 2013. Numerical modeling and experimentation of dynamic Brazilian disc test on Kuru granite. Int. J. Rock Mech. Min. Sci. 59, 128–138.
Schultz, P.H., Eberhardy, C.A., Ernst, C.M., A'Hearn, M.F., Sunshine, J.M., Lisse, C.M., 2007. The Deep Impact oblique impact cratering experiment. Icarus 191, 84–122.
Staehler, J.M., Predebon, W.W., Pletka, B.J., Lankford, J., 1993. Testing of high-strength ceramics with the split Hopkinson pressure bar. J. Am. Ceram. Soc. 76, 536–538.
Tedesco, J.W., Ross, C.A., Kuennen, S.T., 1993. Experimental and numerical analysis of high strain rate splitting-tensile tests. ACI Mater. J. 90, 162–169.
Wang, Q.Z., Li, W., Song, X.L., 2006. A method for testing dynamic tensile strength and elastic modulus of rock materials using SHPB. Pure Appl. Geophys. 163, 1091–1100.
Wang, Q.Z., Li, W., Xie, H.P., 2009. Dynamic split tensile test of Flattened Brazilian Disc of rock with SHPB setup. Mech. Mater. 41, 252–260.
Wong, L.N.Y., Zou, C., Cheng, Y., 2014. Fracturing and failure behavior of carrara marble in quasistatic and dynamic Brazilian disc tests. Rock Mech. Rock Eng. 47, 1117–1133.
Wu, B., Yao, W., Xia, K., 2016. An experimental Study of dynamic tensile failure of rocks subjected to hydrostatic confinement. Rock Mech. Rock Eng. 49, 3855–3864.
Xing, H.Z., Zhang, Q.B., Zhao, J., 2018. Stress thresholds of crack development and poisson's ratio of rock material at high strain rate. Rock Mech. Rock Eng. 51, 945–951.
Yan, F., Feng, X.-T., Chen, R., Xia, K., Jin, C., 2012. Dynamic tensile failure of the rock interface between tuff and basalt. Rock Mech. Rock Eng. 45, 341–348.
Yao, Y., Bonakdar, A., Faber, J., Gries, T., Mobasher, B., 2016. Distributed cracking mechanisms in textile-reinforced concrete under high speed tensile tests. Mater. Struct. 49, 2781–2798.
Zhang, Z.X., Kou, S.Q., Yu, J., Yu, Y., Jiang, L.G., Lindqvist, P.-A., 1999. Effects of loading rate on rock fracture. Int. J. Rock Mech. Min. Sci. 36, 597–611.
Zhang, Q.B., Zhao, J., 2013a. Determination of mechanical properties and full-field strain measurements of rock material under dynamic loads. Int. J. Rock Mech. Min. Sci. 60, 423–439.
Zhang, Q.B., Zhao, J., 2013b. Effect of loading rate on fracture toughness and failure micromechanisms in marble. Eng. Fract. Mech. 102, 288–309.
Zhou, Y.X., Xia, K., Li, X.B., Li, H.B., Ma, G.W., Zhao, J., Zhou, Z.L., Dai, F., 2012. Suggested methods for determining the dynamic strength parameters and mode-I fracture toughness of rock materials. Int. J. Rock Mech. Min. Sci. 49, 105–112.
Zhou, Z., Li, X., Zou, Y., Jiang, Y., Li, G., 2014. Dynamic Brazilian tests of granite under coupled static and dynamic loads. Rock Mech. Rock Eng. 47, 495–505.

Prof. Xiaofeng Li earned his BEng from Wuhan University in 2013, and PhD degree from Institute of Rock and Soil Mechanics, Chinese Academy of Sciences and Monash University in 2019. He was selected for the National Natural Science Fund for Excellent Young Scientists Fund Program (Overseas) and the Hubei Province Innovation Talent Program. His research interests lie in the fields of rock dynamics and computational mechanic sciences with emphasis on the development of the hybrid continuum and discontinuum methods for failure modelling of geomaterials spanning the scale from micro-grain-based heterogeneity (mineral, texture, anisotropy, grain morphology) to macro-in-situ applications (rock faulting, geothermal-induced earthquakes). He is the recipient of the 2021 ROCHA runner-up of the ISRM. He is awarded as future leader of Class 2022 in ARMA. He is the main developer of the opensource continuum-discontinuum code (OpenFDEM, www.openfdem.com), which aims to be a free finite and discrete element kernel with object-oriented architecture for solving multiscale, multiphase and multiphysics (3M) problems that operates on various platforms.